

---

# 3D meshfree magnetohydrodynamics

Stephan Rosswog<sup>1</sup> and Daniel Price<sup>2</sup>

<sup>1</sup> Jacobs University Bremen, Campus Ring 1, D-28759 Bremen, Germany  
s.rosswog@jacobs-university.de

<sup>2</sup> School of Physics, University of Exeter, Stocker Rd, Exeter EX4 4QL, UK  
dprice@astro.ex.ac.uk

**Summary.** We describe a new method to include magnetic fields into smooth particle hydrodynamics. The derivation of the self-gravitating hydrodynamics equations from a variational principle is discussed in some detail. The non-dissipative magnetic field evolution is instantiated by advecting so-called Euler potentials. This approach enforces the crucial  $\nabla \cdot \mathbf{B} = 0$ -constraint by construction. These recent developments are implemented in our three-dimensional, self-gravitating magnetohydrodynamics code MAGMA. A suite of tests is presented that demonstrates the superiority of this new approach in comparison to previous implementations.

**Key words:** astrophysics, magnetohydrodynamics, smoothed particle hydrodynamics, magnetic fields, Euler potentials

## 1 Specific astrophysical requirements

Astrophysical simulations have their specific requirements which differ in many respects from those of other branches of computationally intense research fields. The dynamics of self-gravitating gas masses plays a prominent role throughout astrophysics, but it is usually only one of several ingredients and it is often necessary to account for additional physical processes such as radiative transfer, nuclear burning or the evolution of magnetic fields to address questions of astrophysical interest. These additional processes often involve intrinsic length and time scales that are dramatically different from those of the gas dynamical processes making astrophysical problems prime examples of multi-scale and multi-physics challenges.

Since fixed boundaries are usually absent, flow geometries are determined by the interplay between different physical processes such as gas dynamics and (self-)gravity which often leads to complicated, dynamically changing flow geometries. Therefore, many problems require flexible numerical schemes such as adaptive mesh refinement or completely meshfree, Lagrangian methods. Each of these methods has its strengths and weaknesses and the choice of the

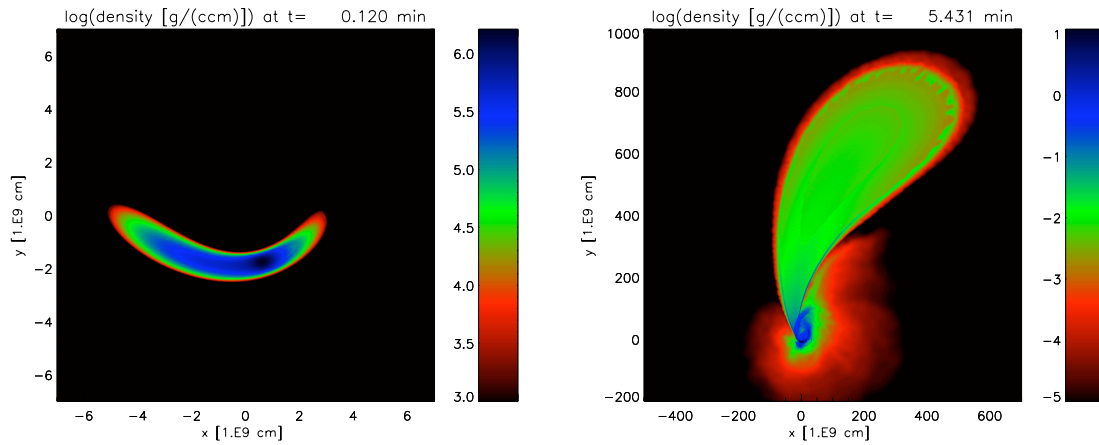


**Figure 1.** Two snapshots from the simulation of the tidal disruption of a white dwarf by a black hole.

best-suited method can usually save a tremendous amount of effort.

An astrophysical example of such an intrinsic multi-scale and multi-physics problem is shown in Fig. 1<sup>3</sup>. It shows two snapshots from a simulation of the tidal disruption of a white dwarf star by a black hole. The initially spherical star becomes strongly distorted while passing the black hole (left panel), it is heavily compressed compressed and shock-heated which triggers very rapid nuclear reactions whose energy release leads to the thermonuclear explosion of

<sup>3</sup> Astrophysical implications of this topic are discussed in [1, 2], details of the numerics can be found in [3]

the white dwarf. In order to follow this process for each of the computational fluid particles a nuclear network [4] is evolved on-the-fly together with the hydrodynamics.

In many astrophysical problems the numerical conservation of physically conserved quantities determines the success and the reliability of a numerical simulation. Consider, for example, a molecular gas cloud that collapses under the influence of its own gravity to form stars. If in the simulation angular momentum is artificially dissipated, say due to too coarse a mesh discretization, a collapsing, self-gravitating portion of gas may form just a single stellar object instead of a multiple system of stars and it will thus produce a qualitatively wrong result. The “exact”<sup>4</sup> conservation of mass, energy, linear and angular momentum is –besides its natural adaptivity– one of the main strengths of the smoothed particle hydrodynamics (SPH) method. This exact conservation can be “hardwired” into SPH’s evolution equations via symmetries in the fluid particle indices. Originally this was done –successfully, but somewhat arbitrarily– by hand[5, 6, 7], but more recently it was shown [8, 9, 10, 11] how the correct symmetries follow elegantly and stringently from a discretized fluid Lagrangian and the Euler-Lagrange variational principle.

In the following, we will review the derivation of the self-gravitating SPH equations from a Lagrangian, see Sect.2.1. We will also discuss in detail how to implement magnetic fields via so-called Euler potentials, see Sect. 2.2. This approach is similar to evolving a vector potential and enforces the crucial  $\nabla \cdot \mathbf{B} = 0$ -constraint which otherwise poses a severe challenge for particle methods. These new developments are implemented in our self-gravitating, three-dimensional magnetohydrodynamics code MAGMA, which is described in Sect. 3.

## 2 Guiding principles

### 2.1 Ideal smoothed particle hydrodynamics (SPH)

The smoothed particle hydrodynamics method (SPH) had originally been developed in the astrophysical context to simulate the formation of stellar binary systems via fission[12] and the structure of non-spherical stars[13]. While the initial 3D simulations used 80 (Gingold and Monaghan) and 100 SPH particles (Lucy) today’s state of the art cosmological SPH simulations have reached particle numbers in excess  $10^9$ , see e.g. [14]. This is only in part due to the increase in hardware performance, also the simulation techniques (in particular the treatment of self-gravity) have become continuously more sophisticated and much effort has been invested to parallelize 3D codes on various computing platforms. Also the formulation of the SPH equations has come a very long

---

<sup>4</sup> “Exact” means up to possible effects from the numerical integration of the resulting ODEs or from using approximative forces, say from a tree or some other Poisson-solver.

way from the initial straight-forward discretisation of the Lagrangian gas dynamics equations to its most recent formulation that follows stringently from a discretized ideal fluid Lagrangian.

Here we will give a brief overview over an older SPH-formulation, but we will mainly focus on an approach that is based on a derivation from a discretised Lagrangian. This latter approach naturally introduces so-called “grad- $h$ ” terms that result from changes in the smoothing lengths of the SPH particles.

### “Vanilla Ice” SPH

The approximation of function values and derivatives via a kernel summation is at the heart of SPH. If the values of a function  $f$  are known at a set of discrete points (“particles”) labelled by  $b$ , the SPH approximation of the function  $f$  at position  $\mathbf{r}$  is given by [6, 7, 15]<sup>5</sup>

$$f(\mathbf{r}) = \sum_b \frac{m_b}{\rho_b} f_b W(\mathbf{r} - \mathbf{r}_b, h), \quad (1)$$

where  $m_b$  is the (usually constant) particle mass,  $\rho_b$  is the mass density and  $W$  is a kernel function whose width is determined by the smoothing length  $h$ . Essentially all astrophysical SPH codes use the cubic spline kernel suggested in [16]. Kernel functions with compact support are preferable since they restrict the SPH-summations to a local set of neighbours. For the conservation properties it is convenient to have “radial” kernels,

$$W(\mathbf{r} - \mathbf{r}_b, h) = W(|\mathbf{r} - \mathbf{r}_b|, h), \quad (2)$$

so that

$$\nabla_a W_{bk} = \nabla_b W_{kb} (\delta_{ba} - \delta_{ka}), \quad (3)$$

and

$$\nabla_a W_{ab} = \frac{\partial W_{ab}}{\partial r_{ab}} \hat{e}_{ab}, \quad (4)$$

where  $\mathbf{r}_{ab} = \mathbf{r}_a - \mathbf{r}_b$ ,  $r_{ab} = |\mathbf{r}_{ab}|$ ,  $W_{ab} = W(\mathbf{r}_{ab}, h)$  and  $\hat{e}_{ab} = \mathbf{r}_{ab}/r_{ab}$ . This immediately leads to

$$\nabla_a W_{ab} = -\nabla_b W_{ab} \quad (5)$$

and

$$\frac{dW_{ab}}{dt} = \mathbf{v}_{ab} \cdot \nabla_a W_{ab}, \quad (6)$$

---

<sup>5</sup> Note that we do not specify at this point which  $h$  is used. For this “vanilla ice” SPH the  $h$  that enters the kernel should be a symmetric combination of the smoothing lengths of the involved particles. This will be explained in more detail below. For simplicity, we are omitting the subscript  $h$  in what follows. We also drop the distinction between the function to be interpolated and the interpolant, i.e. we use the same symbol  $f$  on both sides of the following equation.

with  $\mathbf{v}_{ab} = \mathbf{v}_a - \mathbf{v}_b$  being the velocity difference between particle  $a$  and  $b$ . Eq. (1) can be applied in particular to the mass density itself which then reads

$$\rho(\mathbf{r}) = \sum_b m_b W(\mathbf{r} - \mathbf{r}_b, h). \quad (7)$$

The gradient of a function is approximated in SPH by taking the exact derivative of the approximant:

$$\nabla f(\mathbf{r}) = \sum_b \frac{m_b}{\rho_b} f_b \nabla W(\mathbf{r} - \mathbf{r}_b, h). \quad (8)$$

The most straightforward and historically first taken approach is to apply this set of rules to the Lagrangian form of the ideal hydrodynamics equations:

$$\frac{d\rho}{dt} = -\rho \nabla \cdot \mathbf{v}, \quad (9)$$

$$\frac{d\mathbf{v}}{dt} = -\frac{\nabla P}{\rho} + \mathbf{f}, \quad (10)$$

$$\frac{du}{dt} = \frac{P}{\rho^2} \frac{d\rho}{dt} = -\frac{P}{\rho} \nabla \cdot \mathbf{v}, \quad (11)$$

which express the conservation of mass, momentum and energy. Here,  $P$  is the thermodynamic pressure,  $\mathbf{f}$  abbreviates body forces and  $u$  is the thermal energy per mass.

To briefly illustrate the dependence of conservation on the symmetry of the particle indices let us apply Eq. (8) straightforward to the pressure gradient in Eq. (10) (and assume vanishing body forces) to obtain

$$\frac{d\mathbf{v}_a}{dt} = -\frac{1}{\rho_a} \sum_b \frac{m_b}{\rho_b} P_b \nabla_a W_{ab} \quad (12)$$

for the acceleration of particle  $a$ . This form solves the Euler equation to the order of the method, but it does not conserve the total momentum. Consider the force that particle  $b$  exerts on particle  $a$

$$\mathbf{F}_{ba} = \left( m_a \frac{d\mathbf{v}_a}{dt} \right)_b = -\frac{m_a}{\rho_a} \frac{m_b}{\rho_b} P_b \nabla_a W_{ab} \quad (13)$$

and similarly, the force from particle  $a$  on  $b$

$$\mathbf{F}_{ab} = \frac{m_a}{\rho_a} \frac{m_b}{\rho_b} P_a \nabla_a W_{ab}, \quad (14)$$

where we have used Eq. (5). Since in general  $P_a \neq P_b$ , the sum over all the momentum derivatives,  $\sum_b d(m_b \mathbf{v}_b)/dt$ , does not vanish and therefore the total momentum is not conserved.

This deficiency can be easily cured by expressing the pressure gradient term as

$$\frac{\nabla P}{\rho} = \frac{P}{\rho^2} \nabla \rho + \nabla \left( \frac{P}{\rho} \right). \quad (15)$$

If the gradient formula, Eq. (8), is applied to Eq. (15), the momentum equation reads

$$\frac{d\mathbf{v}_a}{dt} = - \sum_b m_b \left( \frac{P_a}{\rho_a^2} + \frac{P_b}{\rho_b^2} \right) \nabla_a W_{ab}. \quad (16)$$

Because the pressure part of the equations is now manifestly symmetric in  $a$  and  $b$  and  $\nabla_a W_{ab} = -\nabla_b W_{ba}$  the forces are now equal and opposite (“actio=reactio”) and therefore the total momentum is conserved by construction, i.e.  $\sum_a m_a \frac{d\mathbf{v}}{dt} = 0$ .

Similarly, the total angular momentum is conserved since the sum of all torques vanishes:

$$\begin{aligned} \frac{d\mathbf{L}}{dt} &= \sum_{a,b} \mathbf{r}_a \times \mathbf{F}_{ba} = \frac{1}{2} \left( \sum_{a,b} \mathbf{r}_a \times \mathbf{F}_{ba} + \sum_{a,b} \mathbf{r}_a \times \mathbf{F}_{ba} \right) \\ &= \frac{1}{2} \left( \sum_{a,b} (\mathbf{r}_a - \mathbf{r}_b) \times \mathbf{F}_{ba} \right) = 0. \end{aligned} \quad (17)$$

Here the summation indices were relabeled and  $\mathbf{F}_{ab} = -\mathbf{F}_{ba}$  was used. The expression finally vanishes, because the forces between particles act along the line joining them, see Eq. (4).

A suitable energy equation can be constructed from Eq. (11) in a straight forward way. Start from the (adiabatic) first law of thermodynamics

$$\frac{du_a}{dt} = \frac{P_a}{\rho_a^2} \frac{d\rho_a}{dt} \quad (18)$$

and insert

$$\frac{d\rho_a}{dt} = \frac{d}{dt} \left( \sum_b m_b W_{ab} \right) = \sum_b m_b \mathbf{v}_{ab} \cdot \nabla_a W_{ab}, \quad (19)$$

where we have used Eq. (6), to find

$$\frac{du_a}{dt} = \frac{P_a}{\rho_a^2} \sum_b m_b \mathbf{v}_{ab} \cdot \nabla_a W_{ab}. \quad (20)$$

Together with an equation of state the equations (7), (16) and (20) form a complete set of SPH equations.

In the previous derivation it was implicitly assumed that derivatives of the smoothing lengths can be ignored. In a simulation with strongly changing geometry, however, it is advisable to locally adapt the smoothing length. This introduces, in principle, additional terms in the SPH equations. The importance of these extra terms depends very much on the exact application [10, 17].

### The SPH-equations from a Lagrangian, “grad-h” terms

#### *The Lagrangian and the Euler-Lagrange equations*

The SPH equations can be derived by using nothing more than a suitable Lagrangian, the first law of thermodynamics and a prescription on how to obtain the density via summation. The Lagrangian of a perfect fluid [18]

$$L = \int \rho \left( \frac{v^2}{2} - u(\rho, s) \right) dV, \quad (21)$$

with  $s$  being the specific entropy, can be SPH-discretized in a straightforward way:

$$L_{\text{SPH,h}} = \sum_b m_b \left( \frac{v_b^2}{2} - u(\rho_b, s_b) \right). \quad (22)$$

The discretized equations for the fluid are then found by applying the Euler-Lagrange equations

$$\frac{d}{dt} \left( \frac{\partial L}{\partial \mathbf{v}_a} \right) - \frac{\partial L}{\partial \mathbf{r}_a} = 0. \quad (23)$$

The term in brackets yields the canonical particle momentum

$$\frac{\partial L}{\partial \mathbf{v}_a} = m_a \mathbf{v}_a, \quad (24)$$

the potential-type second term in the Lagrangian becomes

$$\frac{\partial L}{\partial \mathbf{r}_a} = - \sum_b m_b \frac{\partial u(\rho_b, s_b)}{\partial \mathbf{r}_a} = - \sum_b m_b \left. \frac{\partial u_b}{\partial \rho_b} \right|_s \cdot \frac{\partial \rho_b}{\partial \mathbf{r}_a}. \quad (25)$$

The first derivative can be expressed using the first law of thermodynamics,  $du = P/\rho^2 d\rho$ , and therefore

$$m_a \frac{d\mathbf{v}_a}{dt} = - \sum_b m_b \frac{P_b}{\rho_b^2} \frac{\partial \rho_b}{\partial \mathbf{r}_a}. \quad (26)$$

#### *The density, its derivatives and the “grad-h”-terms*

We will now address the additional terms resulting from variable smoothing lengths. For a density estimate as “local” as possible we use the smoothing length  $h_a$  in

$$\rho_a = \sum_b m_b W(r_{ab}, h_a). \quad (27)$$

Adaptivity can be reached by evolving the smoothing length according to

$$h_a = \eta \left( \frac{m_a}{\rho_a} \right)^{1/3}, \quad (28)$$

where  $\eta$  is a parameter typically in a range between 1.2 and 1.5[19]. Since  $\rho_a$  and  $h_a$  mutually depend on each other, see Eqs. (27) and (28), an iteration is required for consistency.

If we take the changes of  $h$  into account, the Lagrangian time derivative of the density is given by

$$\begin{aligned} \frac{d\rho_a}{dt} &= \sum_b m_b \left\{ \frac{\partial W_{ab}(h_a)}{\partial r_{ab}} \frac{dr_{ab}}{dt} + \frac{\partial W_{ab}(h_a)}{\partial h_a} \frac{dh_a}{dt} \right\} \\ &= \sum_b m_b \mathbf{v}_{ab} \cdot \nabla_a W_{ab}(h_a) + \frac{\partial h_a}{\partial \rho_a} \frac{d\rho_a}{dt} \sum_b m_b \frac{\partial}{\partial h_a} W_{ab}(h_a), \end{aligned}$$

where we have used  $dr_{ab}/dt = \hat{e}_{ab} \cdot \mathbf{v}_{ab}$  and Eq. (5). If the  $d\rho_a/dt$ -terms are collected into the quantity

$$\Omega_a \equiv \left( 1 - \frac{\partial h_a}{\partial \rho_a} \cdot \sum_b m_b \frac{\partial}{\partial h_a} W_{ab}(h_a) \right), \quad (29)$$

the time derivative of the density reads

$$\frac{d\rho_a}{dt} = \frac{1}{\Omega_a} \sum_b m_b \mathbf{v}_{ab} \cdot \nabla_a W_{ab}(h_a). \quad (30)$$

This is the generalization of the standard SPH expression, Eq. (19). In a similar way the spatial derivatives can be calculated

$$\begin{aligned} \frac{\partial \rho_b}{\partial \mathbf{r}_a} &= \sum_k m_k \left\{ \nabla_a W_{bk}(h_b) + \frac{\partial W_{bk}(h_b)}{\partial h_b} \frac{\partial h_b}{\partial \mathbf{r}_a} \right\} \\ &= \sum_k m_k \nabla_a W_{bk}(h_b) + \frac{\partial h_b}{\partial \rho_b} \frac{\partial \rho_b}{\partial \mathbf{r}_a} \sum_k m_k \frac{\partial W_{bk}(h_b)}{\partial h_b}, \end{aligned}$$

or,

$$\frac{\partial \rho_b}{\partial \mathbf{r}_a} = \frac{1}{\Omega_b} \sum_k m_k \nabla_a W_{bk}(h_b). \quad (31)$$

*The SPH equations with “grad-h”-terms*

Inserting Eq. (30) into Eq. (18) yields the “grad-h” energy equation

$$\frac{du_{a,h}}{dt} = \frac{1}{\Omega_a} \frac{P_a}{\rho_a^2} \sum_b m_b \mathbf{v}_{ab} \cdot \nabla_a W_{ab}(h_a). \quad (32)$$

With the derivative Eq. (31) one can write Eq. (26) as

$$m_a \frac{d\mathbf{v}_a}{dt} = - \sum_b m_b \frac{P_b}{\rho_b^2} \nabla_a \rho_b = - \sum_b m_b \frac{P_b}{\rho_b^2} \left( \frac{1}{\Omega_b} \sum_k m_k \nabla_a W_{bk}(h_b) \right). \quad (33)$$



With Eq. (3), the above equation becomes

$$\begin{aligned} m_a \frac{d\mathbf{v}_a}{dt} &= - \sum_b m_b \frac{P_b}{\rho_b^2} \frac{1}{\Omega_b} \sum_k m_k \nabla_b W_{kb}(h_b) (\delta_{ba} - \delta_{ka}) \\ &= -m_a \sum_b m_b \left( \frac{P_a}{\Omega_a \rho_a^2} \nabla_a W_{ab}(h_a) + \frac{P_b}{\Omega_b \rho_b^2} \nabla_a W_{ab}(h_b) \right), \end{aligned} \quad (34)$$

i.e. the final momentum equation reads

$$\frac{d\mathbf{v}_{a,h}}{dt} = - \sum_b m_b \left( \frac{P_a}{\Omega_a \rho_a^2} \nabla_a W_{ab}(h_a) + \frac{P_b}{\Omega_b \rho_b^2} \nabla_a W_{ab}(h_b) \right). \quad (35)$$

Together with the density equation, Eq. (7), and an equation of state, Eqs. (32) and (35) form a complete set of “grad-h” SPH-equations.

#### *Self-gravity and gravitational softening*

The variational concept can also be applied to derive the gravitational forces including softening in a self-consistent way[20]. If gravity is taken into account, a gravitational part has to be added to the Lagrangian,  $L_{\text{SPH}} = L_{\text{SPH,h}} + L_{\text{SPH,g}}$  with

$$L_{\text{SPH,g}} = - \sum_b m_b \Phi_b, \quad (36)$$

where  $\Phi_b$  is the potential at the particle position  $b$ ,  $\Phi(\mathbf{r}_b)$ . The potential  $\Phi$  can be written as a sum over particle contributions

$$\Phi(\mathbf{r}) = -G \sum_b m_b \phi(|\mathbf{r} - \mathbf{r}_b|, h), \quad (37)$$

and it is related to the matter density by Poisson’s equation

$$\nabla^2 \Phi = 4\pi G \rho. \quad (38)$$

If we insert the sum representations of both the potential, Eq. (37), and the density, Eq. (7), into the Poisson equation, Eq. (38), we obtain a relationship between the gravitational softening kernel,  $\phi$ , and the SPH-smoothing kernel  $W$ :

$$W(|\mathbf{r} - \mathbf{r}_b|, h) = - \frac{1}{4\pi} \frac{\partial}{\partial r} \left( r^2 \frac{\partial}{\partial r} \phi(|\mathbf{r} - \mathbf{r}_b|, h) \right). \quad (39)$$

Here we have used that both  $\phi$  and  $W$  depend only radially on the position coordinate.

Applying the Euler-Lagrange equations, Eq. (23), to  $L_{\text{grav,g}}$  yields the particle acceleration due to gravity [20]

$$\begin{aligned} \frac{d\mathbf{v}_{a,g}}{dt} = & -G \sum_b m_b \left[ \frac{\phi'_{ab}(h_a) + \phi'_{ab}(h_b)}{2} \right] \hat{e}_{ab} \\ & - \frac{G}{2} \sum_b m_b \left[ \frac{\zeta_a}{\Omega_a} \nabla_a W_{ab}(h_a) + \frac{\zeta_b}{\Omega_b} \nabla_a W_{ab}(h_b) \right], \end{aligned} \quad (40)$$

where  $\phi'_{ab} = \partial\phi/\partial|\mathbf{r}_a - \mathbf{r}_b|$ . The first term in Eq. (40) is the gravitational force term usually used in SPH. The second term is due to gradients in the smoothing lengths and contains the quantities

$$\zeta_k \equiv \frac{\partial h_k}{\partial \rho_k} \sum_b m_b \frac{\partial \phi_{kb}(h_k)}{\partial h_k} \quad (41)$$

and the  $\Omega_k$  defined in Eq. (29). Formally, it looks very similar to the pressure gradient terms in Eq. (35) with  $G\zeta_k/2$  corresponding to  $P_k/\rho_k^2$ . As  $\zeta_k$  is a negative definite quantity, these adaptive softening terms act against the gas pressure and therefore tend to increase the gravitational forces. The explicit forms of  $\phi$ ,  $\phi'$  and  $\partial\phi/\partial h$  for the cubic spline kernel can be found in Appendix A of [20].

## 2.2 Ideal magnetohydrodynamics

Magnetic fields pervade the Universe in substantial strengths on all scales [21]. They are observed in intra-cluster media in galaxy clusters [22] as well as in individual galaxies [23]. They are thought to be important for the birth of stars [24], they influence the life of stars e.g. via Sun spots or via controlling the angular momentum evolution during a stellar lifetime [25]. Stellar corpses such as neutron stars make themselves known via their magnetic field as pulsars, in a particular breed of neutron stars, so-called ‘‘magnetars’’ [26], the field reaches gigantic field strengths of the order  $\sim 10^{15}$  Gauss. On the scale of planets, magnetic fields control the magnetospheres that can shield the planet from the lethal cosmic rays, a fact that has certainly facilitated the evolution of life on our planet.

### Basic equations of ideal MHD

Magnetohydrodynamics is a one-fluid model for a highly conducting plasma. It assumes that electromagnetic fields are highly coupled to the electron-ion component so that if the fields have a typical frequency  $\omega$  and wave number  $k$ , they fulfill  $\omega\tau_h \sim 1$  and  $k\lambda_h \sim 1$ , where  $\tau_h$  and  $\lambda_h$  are the typical hydrodynamic time and length scales. If

$$\frac{1}{\beta_{\text{plas}}} \left( \frac{r_{L_i}}{\lambda_h} \right)^2 \ll \left( \frac{m_i}{m_e} \right)^{1/2} \left( \frac{\tau_i}{\tau_h} \right) \ll 1, \quad (42)$$

where  $\beta_{\text{plas}}$  is the ratio between gas and magnetic pressure,  $r_{L_i}$  the Larmor radius of the ions,  $m_i$  and  $m_e$  the ion and electron masses and  $\tau_i$  is the typical

ion collision time, is fulfilled, the plasma can be described by the equations of ideal magnetohydrodynamics[27]:

$$\frac{d\rho}{dt} = -\rho \nabla \cdot \mathbf{v} \quad (43)$$

$$\frac{dv^i}{dt} = \frac{1}{\rho} \frac{\partial S^{ij}}{\partial x^j} \quad (44)$$

$$\frac{du}{dt} = -\frac{P}{\rho} \nabla \cdot \mathbf{v} \quad (45)$$

$$\frac{d\mathbf{B}}{dt} = -\mathbf{B}(\nabla \cdot \mathbf{v}) + (\mathbf{B} \cdot \nabla)\mathbf{v}, \quad (46)$$

where the magnetic stress tensor is given by

$$S^{ij} = -P\delta^{ij} + \frac{1}{\mu_0} \left( B^i B^j - \frac{1}{2} B^2 \delta^{ij} \right) \quad (47)$$

and the  $B^k$  are the components of the magnetic field strength. Note that for ideal magnetohydrodynamics only the momentum equation has to be modified, the energy and the continuity equation are identical to the case of vanishing magnetic field. The form of the momentum equation employed here formally accounts for  $\mathbf{B}(\nabla \cdot \mathbf{B})$  terms which are needed for momentum conservation in shocks but on the other hand can be the cause of numerical instabilities, see [28] for a detailed discussion.

Due to its relative simplicity in comparison to a more sophisticated plasma treatment magnetohydrodynamics and in particular ideal magnetohydrodynamics has been employed throughout a broad range of applications with sometimes not sufficient consideration about its range of applicability. Whether the conditions of applicability [29, 27] really hold needs to be checked for each problem individually.

### Euler potentials

Being dissipationless the ideal MHD equations are conservative which leads to some important implications, the most powerful of which is probably the *frozen flux theorem* [30] which states that the magnetic field is carried around by the plasma. This kinematic effect is due to the evolution equation of the magnetic field, Eq. (46), and represents the conservation of magnetic flux through a fluid element. In reality, i.e. in the presence of dissipative terms, some slippage between the magnetic field and the plasma will occur.

The idea that the magnetic field lines are carried around by the flow is closely related to the concepts of Euler potentials [31] which are sometimes also referred to as Clebsch variables. For a review on Euler potentials we refer to [32, 33]. The basic idea is to present the magnetic field by two scalar variables,  $\alpha$  and  $\beta$  such that

$$\mathbf{B} = \nabla\alpha \times \nabla\beta. \quad (48)$$

From this definition it is obvious that

$$\mathbf{B} \cdot \nabla\alpha = 0 = \mathbf{B} \cdot \nabla\beta, \quad (49)$$

in other words:  $\alpha$  and  $\beta$  are constant along each field line and can therefore be used as field line labels. This is graphically represented in Fig. 2. The frozen

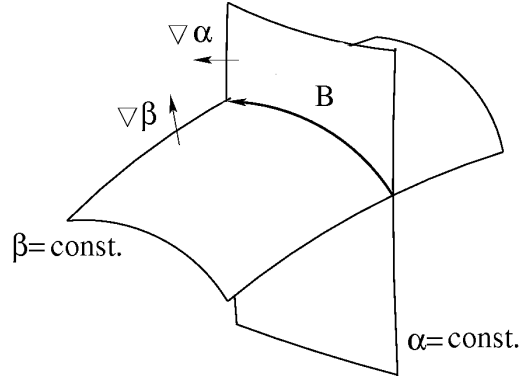


**Figure 2.** The intersection of a plane of constant  $\alpha$  with a plane of constant  $\beta$  labels a magnetic field line.

flux property of ideal MHD the simply translates into advecting  $\alpha$  and  $\beta$  with a Lagrangian fluid element:

$$\frac{d\alpha_a}{dt} = 0 \quad \text{and} \quad \frac{d\beta_a}{dt} = 0. \quad (50)$$

The Euler potentials naturally relate to the magnetic vector potential via

$$\mathbf{A} = \alpha\nabla\beta + \nabla\xi \quad (51)$$

or

$$\mathbf{A} = -\beta\nabla\alpha + \nabla\psi, \quad (52)$$

where  $\xi$  and  $\psi$  are arbitrary smooth functions. It is straightforward to check that both of the above forms of the vector potential yield the magnetic field via

$$\nabla \times \mathbf{A} = \nabla\alpha \times \nabla\beta = \mathbf{B}. \quad (53)$$

Thus, the  $\nabla \cdot \mathbf{B} = 0$ -constraint that is otherwise very hard to fulfill in a particle method [34, 19, 35] can be hard-wired into the numerical scheme by using the

advected quantities  $\alpha$  and  $\beta$  to construct the magnetic field via Eq. (48). This approach has the additional ease that, as long as the magnetic field is not strong enough to substantially influence the dynamics of the plasma, i.e. in the high- $\beta_{\text{plas}}$ -case, the evolution of different initial field configurations can be explored by just re-processing an existing simulation with different initial values for  $\alpha$  and  $\beta$ . To find Euler potential pairs for a given magnetic field configuration is however usually a non-trivial task due to the non-linear nature of Eq. (48). The Euler potentials for a dipole field are known, but for more complicated field geometries its usually a challenge to find an analytical expression for the Euler potentials. There are however numerical procedures to find suitable pairs of Euler potentials, see e.g. [36, 37].

In two dimensions, a magnetic field can be represented by

$$\alpha = A_z \quad \beta = z, \quad (54)$$

where  $A_z$  is the  $z$ -component of a vector potential.

### Limitations of the Euler potential approach

While the Euler potential approach makes some otherwise rather challenging problems such as magnetic field advection (see below) a trivial task, they have their own difficulties and limitations.

First, the Euler potentials for a given field configuration are not uniquely determined [33]. Assume, for example, that one particular set of Euler potentials,  $\alpha_1$  and  $\beta_1$ , is known. Then for a second set that is a function of the known ones,  $\alpha_2 = \alpha_2(\alpha_1, \beta_1)$  and  $\beta_2 = \beta_2(\alpha_1, \beta_1)$ , one finds

$$\nabla\alpha_2 \times \nabla\beta_2 = \left( \frac{\partial\alpha_2}{\partial\alpha_1} \frac{\partial\beta_2}{\partial\beta_1} - \frac{\partial\beta_2}{\partial\alpha_1} \frac{\partial\alpha_2}{\partial\beta_1} \right) \nabla\alpha_1 \times \nabla\beta_1 \quad (55)$$

and therefore  $\alpha_2$  and  $\beta_2$  will also be a set of Euler potentials for the same field as long as the term in brackets is equal to unity.

Second, by their very nature the Euler potentials are restricted to the purely non-dissipative case and thus they are not immediately suited to treat the case of dissipative effects in a plasma.

Third, there are restrictions with respect to the magnetic field geometries that can be represented by Euler potentials. It is, for example, impossible to represent a linked poloidal and toroidal field. Nevertheless, as will be demonstrated in Sec.3.3, on a large set of standard MHD-test problems the Euler potential approach yields excellent results.

From a numerical point of view they involve higher-order derivatives, see Eqs. (44) and (48) which is usually numerically challenging. However, as will be shown below, this not necessarily has to degrade the accuracy of the solution.

### 2.3 Dissipative terms

In both hydrodynamics and magnetohydrodynamics we are interested in principle in the non-dissipative cases, see Sec. 2.1 and 2.2. The corresponding equations, however, allow for discontinuous shock solutions which need to be captured in order to allow for a physically correct and numerically stable solution. This can be done by either making use of the analytical solution by locally solving a Riemann-type problem or by artificially spreading the discontinuities to a numerically resolvable width which means making them continuous. This latter artificial viscosity approach is most often used in the context of smooth particle hydrodynamics, although Riemann-solver-type approaches also do exist [38, 39].

A careful design of artificial dissipation terms is essential to capture physically correct solutions. This was recently demonstrated at the example of Kelvin-Helmholtz instabilities [40]. In the design of artificial dissipation terms we are guided by two principles: a) we want to use a form of the artificial dissipation equations that is oriented at Riemann-solvers [41] and b) we aim at applying dissipative terms only where they are necessary, i.e. near discontinuities, and follow in this respect Morris and Monaghan [42] who suggested to use time dependent dissipation parameters.

Based on the analogy with Riemann solvers Monaghan [41] presented a general formulation of dissipative terms. It was noted that the evolution equations of every conservative quantity should contain dissipative terms to control discontinuities. This approach has been applied to ultra-relativistic [43] and magnetohydrodynamic shocks [35]. The “discontinuity capturing” term for a variable  $A$  is of the form

$$\left(\frac{dA}{dt}\right)_{a,\text{diss}} = \sum_b m_b \frac{\alpha_A v_{\text{sig},A}}{\rho_{ab}} (A_a - A_b) \hat{e}_{ab} \cdot \nabla W_{ab}, \quad (56)$$

where  $\alpha_A$  is a number of order unity that specifies the exact amount of dissipation,  $v_{\text{sig},A}$  is an appropriate signal velocity and  $\rho_{ab}$  the average mass density of particles  $a$  and  $b$ .

A comparison with the SPH expression for Laplacians [44] shows that the above equation is really an expression for [40]

$$\left(\frac{dA}{dt}\right)_{a,\text{diss}} = \eta \nabla^2 A \quad (57)$$

with  $\eta \propto \alpha_A v_{\text{sig}} |r_{ab}|$ .

Following [42] the parameter that determines the exact values of the dissipative parameters,  $\alpha_A$ , is made time-dependent. This is put into effect by integrating an additional differential equation containing both a source term,  $S_A$ , that indicates the necessity of artificial dissipation and a decay term that contains the typical time scale,  $\tau_A$ , it takes a particle to pass the discontinuity. The evolution equation of the dissipation parameter is given by

$$\frac{d\alpha_{A,a}}{dt} = -\frac{\alpha_{A,a} - \alpha_{\min}}{\tau_{A,a}} + S_{A,a}, \quad (58)$$

where  $\alpha_{\min}$  is the minimum value to which we allow  $\alpha_A$  to decay. The decay time scale is given by

$$\tau_{A,a} = \frac{h_a}{C v_{\text{sig},A}}, \quad (59)$$

where  $C$  is a constant of order unity that is chosen after careful numerical experiments at problems with analytically known solutions.

### 3 The MAGMA code

Collisions between stars are very rare events in the solar neighbourhood. Close to centres of galaxies and globular clusters, however, the number densities of stars are higher by up to a factor of  $10^6$  [45] and therefore stellar collisions are very common events. In fact, the innermost 0.3 lightyears of our Galaxy can be considered an efficient “stellar collider” [46]. A different type of encounter can occur for stellar binary systems that contain compact stellar objects. If born at close enough separations such systems can be driven towards merger by the emission of gravitational waves. Although rare per space volume these types of encounters release tremendous amounts of gravitational energy and are therefore potentially visibly out to cosmological distances thereby making huge volumes observationally accessible and producing a substantial observational rate.

Some of the most exciting astrophysical objects are thought to form in such encounters and since both neutron stars and white dwarfs are known to be threaded by very large magnetic fields, a careful study of such mergers requires the inclusion of magnetic fields and their evolution.

#### 3.1 Scope and physics modules

The acronym MAGMA stands for *a magnetohydrodynamics code for merger applications* and this code has originally been developed for the study of magnetized neutron stars [47, 48]. A very detailed description of this code can be found in [17].

For astrophysical studies the code contains several physics modules that go beyond the scope of this article and shall only be briefly sketched here. The interested reader is referred to the astrophysical literature.

##### *Equation of state*

For the thermodynamic properties of neutron star matter we use a temperature-dependent relativistic mean-field equation of state [49, 50]. It can handle temperatures from 0 to 100 MeV<sup>6</sup>, electron fractions from  $Y_e = 0$  (pure neutron

<sup>6</sup> 1 MeV corresponds to  $1.16 \cdot 10^{10}$  K.

matter) up to 0.56 and densities from about 10 to more than  $10^{15}$  g cm $^{-3}$ . No attempt is made to include matter constituents that are more exotic than neutrons and protons at high densities. For more details we refer to [51].

#### *Neutrino emission*

The code contains a detailed multi-flavor neutrino leakage scheme. An additional mesh is used to calculate the neutrino opacities that are needed for the neutrino emission rates at each particle position. The neutrino emission rates are used to account for the local cooling and the compositional changes due to weak interactions such as electron captures. A detailed description of the neutrino treatment can be found in [52].

#### *Self-gravity*

The self-gravity of the fluid is treated in a Newtonian fashion. Both the gravitational forces and the search for the particle neighbors are performed with a binary tree that is based on the one described in [53]. These tasks are the computationally most expensive part of the simulations and in practice they completely dominate the CPU-time usage. Forces emerging from the emission of gravitational waves are treated in a simple approximation. For more details, we refer to the literature [54, 51].

### 3.2 The MAGMA equations

Here, we will only briefly summarize the implemented equations, the explicit forms of all the equations can be found in [17].

Instead of explicitly integrating the continuity equation, we calculate the density via summation as in Eq. (7). The momentum equation is used in the form

$$\frac{d\mathbf{v}_{a,\text{MHD}}}{dt} = \frac{d\mathbf{v}_{a,\text{h}}}{dt} + \frac{d\mathbf{v}_{a,\text{h,diss}}}{dt} + \frac{d\mathbf{v}_{a,\text{g}}}{dt} + \frac{d\mathbf{v}_{a,\text{mag}}}{dt} + \frac{d\mathbf{v}_{a,\text{mag,diss}}}{dt} \quad (60)$$

where  $d(\mathbf{v}_{a,\text{h}})/dt$  is given in Eq. (35),  $d(\mathbf{v}_{a,\text{g}})/dt$  is given in Eq. (40), and the explicit forms of the dissipative terms,  $d(\mathbf{v}_{a,\text{h,diss}})/dt$  and  $d(\mathbf{v}_{a,\text{mag,diss}})/dt$ , can be found in [17]. The magnetic force term is used in the form

$$\begin{aligned} \frac{d\mathbf{v}_{a,\text{mag}}}{dt} = & - \sum_b \frac{m_b}{\mu_0} \left\{ \frac{B_a^2/2}{\Omega_a \rho_a^2} \nabla_a W_{ab}(h_a) + \frac{B_b^2/2}{\Omega_b \rho_b^2} \nabla_a W_{ab}(h_b) \right\} \\ & + \sum_b \frac{m_b}{\mu_0} \left\{ \frac{\mathbf{B}_a(\mathbf{B}_a \cdot \overline{\nabla_a W_{ab}}) - \mathbf{B}_b(\mathbf{B}_b \cdot \overline{\nabla_a W_{ab}})}{\rho_a \rho_b} \right\}, \end{aligned} \quad (61)$$

where the symmetrized kernel gradient is given by

$$\overline{\nabla_a W_{ab}} = \frac{1}{2} \left[ \frac{1}{\Omega_a} \nabla_a W_{ab}(h_a) + \frac{1}{\Omega_b} \nabla_a W_{ab}(h_b) \right]. \quad (62)$$



The magnetic field is calculated from the Euler potentials<sup>7</sup>. Note that another form of the magnetic force term is also possible [35, 17]. The gradients of the Euler potentials are calculated in a way that gradients of linear functions are reproduced exactly [19, 17]. To handle magnetic shocks artificial dissipation terms were constructed according to the ideas outlined in Sec. 2.3. They are also applied to the evolution of  $\alpha_a$  and  $\beta_a$ . They are not meant to mimic physical dissipation in any way, their exclusive aim is to keep gradients numerically treatable.

The MAGMA energy equation is of the form

$$\frac{du_{a,\text{MHD}}}{dt} = \frac{du_{a,\text{h}}}{dt} + \frac{du_{a,\text{AV}}}{dt} + \frac{du_{a,\text{C}}}{dt}, \quad (63)$$

where  $d(u_{a,\text{h}})/dt$  is given in Eq. (32), the explicit form of the artificial viscosity term  $d(u_{a,\text{AV}})/dt$  and the thermal conductivity term  $d(u_{a,\text{C}})/dt$  can be found in [17].

### 3.3 Tests and benchmarks

We present here a selection of standard tests used in the hydro- and magnetohydrodynamics community to validate numerical schemes. For a more exhaustive set of benchmarks we refer to [17].

#### Hydrodynamics

##### *1D: Sod's shock tube*

As a standard test of the shock capturing capability we show the results of Sod's shock tube test [55]. To the left of the origin, the initial state of the fluid is given by  $[\rho, P, v_x]_{\text{L}} = [1.0, 1.0, 0.0]$  whilst to the right of the origin the initial state is  $[\rho, P, v_x]_{\text{R}} = [0.125, 0.1, 0.0]$  with  $\gamma = 1.4$ . The problem is setup using 900 equal mass particles in one spatial dimension. Rather than adopting the usual practice of smoothing the initial conditions across the discontinuity, we follow [19] in using unsmoothed initial conditions but applying a small amount of artificial thermal conductivity. The results are shown in Figure 3, where the points represent the SPH particles. For comparison the exact solution computed using a Riemann solver is given by the solid line.

The shock itself is smoothed by the artificial viscosity term, which in this case can be seen to spread the discontinuity over about 6 particles. The contact discontinuity is smoothed by the application of artificial thermal conductivity which (in particular) eliminates the ‘‘wall heating’’ effect often visible in numerical solutions to this problem. The exact distribution of particle separations in the contact discontinuity seen in Figure 3 is related to the initial particle placement across the discontinuity.

<sup>7</sup> Note that the code also allows to evolve magnetic fields according to a more straightforward SPH discretisation [35].

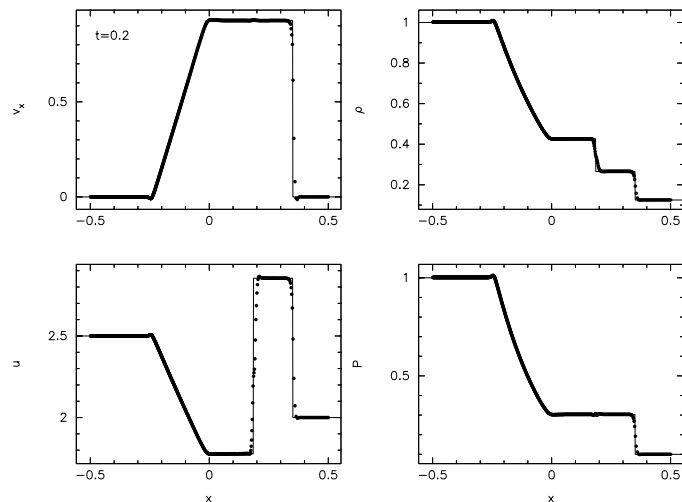


**Figure 3.** Results of the Sod shock tube test in one dimension using 900 SPH particles setup using unsmoothed initial conditions. Artificial viscosity and thermal conductivity are applied to appropriately smooth the shock and contact discontinuity respectively. The exact solution is given by the solid line. The upper row displays the velocity (left) and the density (right), the bottom row shows specific internal energy (left) and the pressure (right).

For this test, applying artificial viscosity and thermal conductivity as described, we do not find a large difference between the “grad- $h$ ” formulation and other variants of SPH based on averages of the smoothing length. If anything, the “grad- $h$ ”-terms tend to increase the order of the method, which, as in any higher order scheme, tends to enhance oscillations which may otherwise be damped, visible in Figure 3 as small “bumps” at the head of the rarefaction wave (in the absence of artificial viscosity these bumps appear as small but regular oscillations with a wavelength of a few particle spacings).

### *3D: Sedov blast wave test*

In order to demonstrate that our scheme is capable of handling strong shocks in three dimensions, we have also tested the code on a Sedov blast wave problem both with, see Sec. 3.3, and without magnetic fields. Without magnetic fields the explosion is spherically symmetric, however for a strong magnetic field the blast wave is significantly inhibited perpendicular to the magnetic field lines, resulting in a compression along one spatial dimension. Similar tests for both hydrodynamics and MHD have been used by many authors – for example by [56] in order to benchmark an Adaptive Mesh Refinement (AMR) code for MHD and by [57] in benchmarking the cosmological SPH

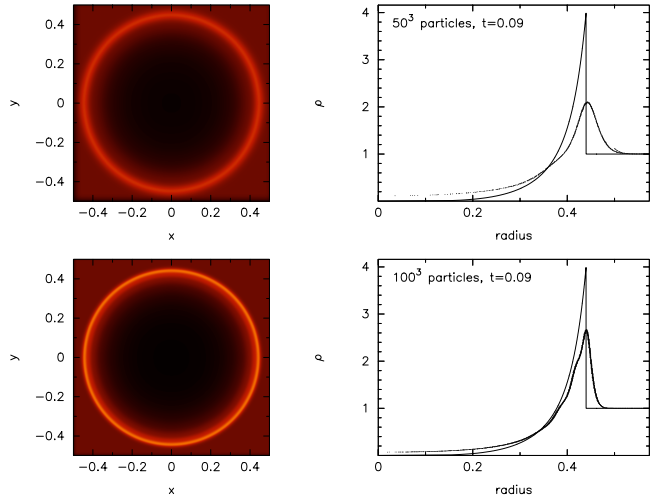


**Figure 4.** Results of the hydrodynamic Sedov blast wave test in 3D at  $t = 0.09$  at resolutions of 125,000 (top) and 1 million (bottom) particles respectively. The density and radial position of each SPH particle are shown in each case, which may be compared to the exact solution given by the solid line.

code GADGET.

The hydrodynamic version is set up as follows: The particles are placed in a cubic lattice configuration in a three dimensional domain  $[-0.5, 0.5] \times [-0.5, 0.5] \times [-0.5, 0.5]$  with uniform density  $\rho = 1$  and zero pressure and temperature apart from a small region  $r < R$  near the origin, where we initialize the pressure using the total blast wave energy  $E = 1$ , ie.  $P = (\gamma - 1)E / (\frac{4}{3}\pi R^3)$ . We set the initial blast radius to the size of a single particle’s smoothing sphere  $R = 2\eta\Delta x$  (where 2 is the kernel radius,  $\eta (= 1.5)$  is the smoothing length in units of the average particle spacing as in Eq. (28) and  $\Delta x$  is the initial particle spacing on the cubic lattice) such that the explosion is as close to point-like as resolution allows. Boundaries are not important for this problem, however we use periodic boundary conditions to ensure that the particle distribution remains smooth at the edges of the domain.

The results shown in Figure 4 at  $t = 0.09$  have been obtained with a resolution of 50 and 100 particles<sup>3</sup> (ie. 125,000 and 1 million particles respectively), where we have plotted (left panels) the density in a  $z = 0$  cross section slice and (right panels) the density and radial position of each particle (dots) together with the exact self-similar Sedov solution (solid line).

We found that the key to an accurate simulation of this problem in SPH is to incorporate an artificial thermal conductivity term due to the huge initial discontinuity in thermal energy. The importance of such a term for shock

problems in SPH has been discussed recently by [19, 40]. In the absence of this term the particle distribution quickly becomes disordered around the shock front and the radial profile appears to be noisy. From Figure 4 we see that at a resolution of 1 million particles the highest density in the shock at  $t = 0.09$  is  $\rho_{\max} = 2.67$  whereas for the lower resolution run  $\rho_{\max} = 2.1$ , consistent with a factor of 2 change in smoothing length. Using this we can estimate that a resolution of  $\sim 345^3 = 41$  million particles is required to fully resolve the density jump in this problem in three dimensions. Note that the minimum density obtained in the post-shock rarefaction also decreases with resolution. Some small-amplitude post-shock oscillations are visible in the solution which we attribute to interaction of the spherical blast wave with particles in the surrounding medium initially placed on a regular (Cartesian) cubic lattice.

## Magnetohydrodynamics

### *1D: Brio-Wu shock tube test*

The magnetic shock tube test of [58] has become a standard test case for numerical MHD schemes that has been widely used by many authors to benchmark (mainly grid-based) MHD codes [59, 60, 61, 62]. The Brio-Wu shock test is the MHD analogon to Sod’s shock tube problem that was described earlier, but here no analytical solution is known. The MHD Riemann problem allows for much more complex solutions than the hydrodynamic case which can occur because of the three different types of waves (i.e. slow, fast and Alfvén, compared to just the sound waves in hydrodynamics). In the Brio-Wu shock test the solution contains the following components (from left to right in Fig. 5): a fast rarefaction fan and a slow compound wave consisting of a slow rarefaction attached to a slow shock (moving to the left) and a contact discontinuity, a slow shock and a fast rarefaction fan (moving to the right). It has been pointed out, however, that the stability of the unusual compound wave may be an artifact of the restriction of the symmetry to one spatial dimension whilst allowing the magnetic field to vary in two dimensions, [63]. The shown results are obtained using Euler potential formulation. Results of this problem using Smoothed Particle Magnetohydrodynamics (SPMHD) have been presented elsewhere [28, 19]. The Euler potentials show a distinct improvement over the standard SPMHD results. The initial conditions on the left side of the discontinuity are  $[\rho, P, v_x, v_y, B_y]_{\text{L}} = [1, 1, 0, 0, 1]$  and  $[\rho, P, v_x, v_y, B_y]_{\text{R}} = [0.125, 0.1, 0, 0, -1]$  on the right side. The  $x$ -component of the magnetic field is  $B_x = 0.75$  everywhere and a polytropic exponent of  $\gamma = 2.0$  is used. Using the Euler potentials the components are given by  $\alpha = -B_y x$  (equivalent to the vector potential  $A_z$ ) and  $\beta = z$  (or more specifically  $\nabla\beta = \hat{\mathbf{z}}$ ) and the  $B_x$  component is treated as an external field which requires adding a source term to the evolution equation for  $\alpha$ . Particles are restricted to move in one spatial dimension only, whilst the magnetic field is allowed to vary in two dimensions (that is, we compute a  $v_y$  but do not use it to move the particles).

We setup the problem using 631 equal mass particles in the domain  $x \in [-0.5, 0.5]$  using, as in the hydrodynamic case, purely discontinuous initial conditions. Artificial viscosity, thermal conductivity and resistivity are applied. The results are shown at  $t = 0.1$  in Figure 5. For comparison the numerical solution from [62] is given by the solid line (no exact solution exists for this problem). The solution is generally well captured by our numerical scheme. Two small defects are worth noting. The first is that a small offset is visible in the thermal energy – this is a result of the small non-conservation introduced by use of the Morris formulation [34] of the magnetic force, Eq. (61). Secondly, the rightmost discontinuity is somewhat over-smoothed by the artificial resistivity term. We attribute this to the fact that the dissipative terms involve simply the maximum signal velocity  $v_{sig}$  (that is the maximum of all the wave types). Ideally each discontinuity should be smoothed taking account of it’s individual characteristic and corresponding  $v_{sig}$  (as would occur in a Godunov-MHD scheme). Increasing the total number of particles also decreases the smoothing applied to this wave.

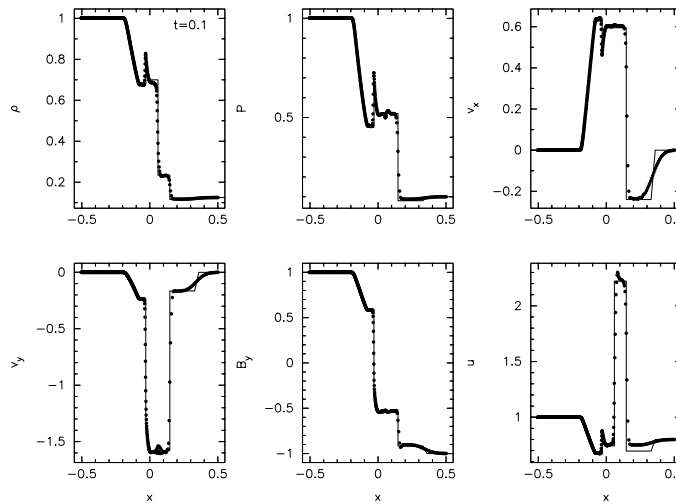


**Figure 5.** Results of the Brio & Wu MHD shock tube test at  $t = 0.1$  using 631 particles and the Euler potential formulation. For comparison the numerical solution taken from [62] is given by the solid line. The solution illustrates the complex shock structures which can be formed due to the different wave types in MHD, including in this case a compound wave consisting of a slow shock attached to a rarefaction wave.

#### *2D: Current loop advection problem*

A simple test problem for MHD is to compute the advection of a weak mag-

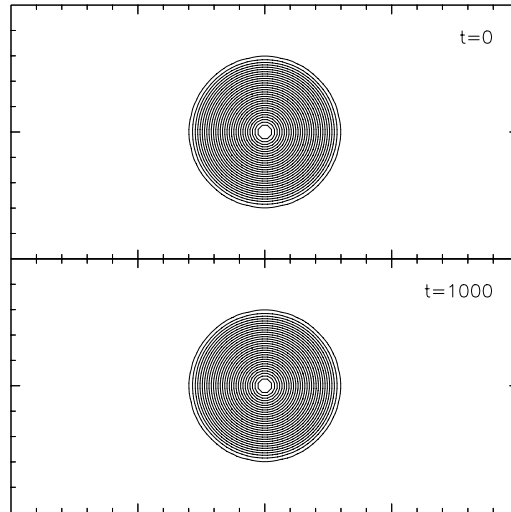


**Figure 6.** Magnetic field lines in the current loop advection test, plotted at  $t = 0$  (top) and after 1000 crossings of the computational domain (bottom).

netic field loop. This test, introduced by [64] in the development of the *Athena* MHD code<sup>8</sup>, presents a challenging problem for grid-based MHD schemes requiring careful formulation of the advection terms in the MHD equations. For our Lagrangian scheme, this test is straightforward to solve which strongly highlights the advantage of using a particle method for MHD in problems where there is significant motion with respect to a fixed reference frame.

We setup the problem following [64]: the computational domain is two dimensional with  $x \in [-1, 1]$ ,  $y \in [-0.5, 0.5]$  using periodic boundary conditions. Density and pressure are uniform with  $\rho = 1$  and  $P = 1$ . The particles are laid down in a cubic lattice configuration with velocity initialized according to  $\mathbf{v} = (v_0 \cos \theta, v_0 \sin \theta)$  with  $\cos \theta = 2/\sqrt{5}$ ,  $\sin \theta = 1/\sqrt{5}$  and  $v_0 = 1$  such that by  $t = 1$  the field loop will have been advected around the computational domain once. The magnetic field is two dimensional, initialized using a vector potential given by

$$A_z = \begin{cases} A_0(R - r) & r \leq R, \\ 0 & r > R, \end{cases} \quad (64)$$

where  $A_0 = 10^{-3}$ ,  $R = 0.3$  and  $r = \sqrt{x^2 + y^2}$ . The ratio of thermal to magnetic pressure is thus given by  $\beta_{\text{plas}} = P/(\frac{1}{2}B^2) = 2 \times 10^6$  (for  $r < R$ ) such that the magnetic field is passively advected. [64] show the results of this problem after two crossings of the computational domain, by which time the loop has either been significantly diffused or has disintegrated into oscillations

<sup>8</sup> <http://www.astro.princeton.edu/~jstone/athena.html>

depending on details of their particular choice of scheme. The advantages of a Lagrangian scheme are that advection is computed exactly, and using our Euler potential formulation for the magnetic field (which in two dimensions is equivalent to a vector potential formulation with  $\alpha = A_z$  and  $\beta = z$ ), this is also true for the evolution of the magnetic field. The result is that the field loop is advected *without change* by our code for as long as one may care to compute it. This is demonstrated in Fig. 6 which shows the magnetic field lines at  $t = 0$  (top) and after 1000 (!) crossings of the computational domain (bottom), in which the field configuration can be seen to be identical to the top figure. The magnetic energy (not shown) is also maintained exactly, whereas [64] find of order a 10% reduction in magnetic energy after two crossings of the domain.

In a realistic simulation involving MHD shocks there will be some diffusion of the magnetic field introduced by the addition of artificial diffusion terms, which are required to resolve discontinuities in the magnetic field. However the point is that these terms are explicitly added to the SPH calculation and can be turned off where they are not necessary whereas the diffusion present in a grid-based code is intrinsic and always present.

#### *2D: Orszag-Tang test*

The evolution of the compressible Orszag-Tang vortex system [65] involves the interaction of several shock waves traveling at different speeds. Originally studied in the context of incompressible MHD turbulence, it has later been extended to the compressible case [66, 67]. It is generally considered a good test to validate the robustness of numerical MHD schemes. In the SPH context, this test has been discussed in detail by [19] and [35].

The problem is two dimensional with periodic boundary conditions on the domain  $[0, 1] \times [0, 1]$ . The setup consists of an initially uniform state perturbed by periodic vortices in the velocity field, which, combined with a doubly periodic field geometry, results in a complex interaction between the shocks and the magnetic field.

The velocity field is given by  $\mathbf{v} = v_0[-\sin(2\pi y), \sin(2\pi x)]$  where  $v_0 = 1$ . The magnetic field is given by  $\mathbf{B} = B_0[-\sin(2\pi y), \sin(4\pi x)]$  where  $B_0 = 1/\sqrt{4\pi}$ . Using the Euler potentials this corresponds to  $\alpha \equiv A_z = B_0/(2\pi)[\cos(2\pi y) + \frac{1}{2}\cos(4\pi x)]$ . The flow has an initial average Mach number of unity, a ratio of magnetic to thermal pressure of 10/3 and we use a polytropic exponent  $\gamma = 5/3$ . The initial gas state is therefore  $P = 5/3B_0^2 = 5/(12\pi)$  and  $\rho = \gamma P/v_0 = 25/(36\pi)$ . Note that the choice of length and time scales differs slightly between various implementations in the literature. The setup used above follows that of [61] and [68].

We compute the problem using  $512 \times 590$  particles initially placed on a uniform, close-packed lattice. The density at  $t = 0.5$  is shown in Figure 7 using both the SPMHD formalism of [35] (left), and the Euler potential approach (right) outlined in Sec.2.2. The Euler potential formulation is clearly superior to the standard SPMHD method. This is largely a result of the relative

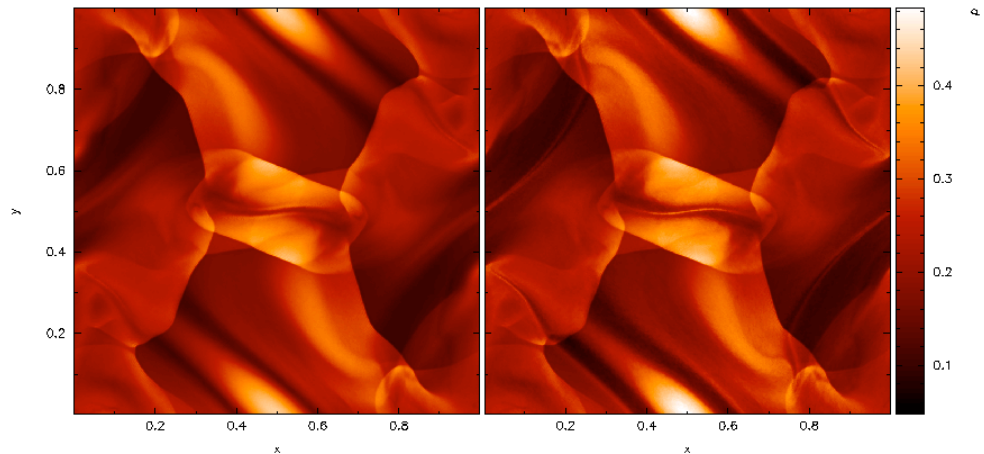


**Figure 7.** Density distribution in the two dimensional Orzsag-Tang vortex problem at  $t = 0.5$ . The initial vortices in the velocity field combined with a doubly periodic field geometry lead to a complex interaction between propagating shocks and the magnetic field. Results are shown using  $512 \times 590$  particles using a SPMHD formalism of [35] (left) and using the Euler potentials (right). The reduced artificial resistivity required in the Euler potential formalism leads to a much improved effective resolution.

requirements for artificial resistivity in each case. In the standard SPMHD method the application of artificial resistivity is crucial for this problem (that is, in the absence of artificial resistivity the density and magnetic field distributions are significantly in error). Using the Euler potentials we find that the solution can be computed using zero artificial resistivity, relying only on the “implicit smoothing” present in the computation of the magnetic field using SPH operators. This means that topological features in the magnetic field are much better preserved, which is reflected in the density distribution. For example the filament near the center of the figure is well resolved using the Euler potentials but completely washed out by the artificial resistivity in the standard SPMHD formalism. Also the high density features near the top and bottom of the figure (coincident to a reversal in the magnetic field) are much better resolved using the Euler potentials.

### *3D: MHD blast wave*

The MHD version of the Sedov test is identical to the hydrodynamic test with the addition of a uniform magnetic field in the  $x$ -direction, that is  $\mathbf{B} = [B_0, 0, 0]$  with  $B_0 = 3.0$ . Initially the surrounding material has zero thermal pressure, meaning that the plasma  $\beta_{\text{plas}}$  is zero (ie. magnetic pressure infinitely strong compared to thermal pressure). However, this choice of field strength



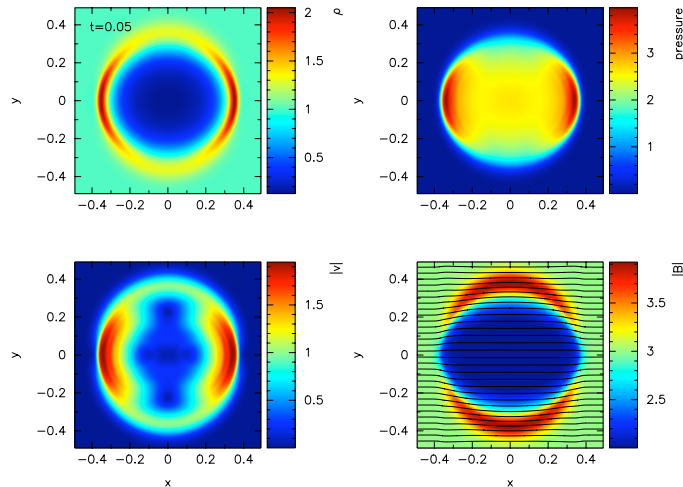


**Figure 8.** Results of the 3D MHD blast wave test at  $t = 0.05$  at a resolution of 1 million ( $100^3$ ) particles. Plots show (left to right, top to bottom) density, pressure, magnitude of velocity and magnetic field strength (with overlaid field lines), plotted in a cross-section slice through the  $z = 0$  plane.

gives a mean plasma  $\beta_{\text{plas}}$  in the post-shock material of  $\beta_{\text{plas}} \sim 1.3$ , such that the magnetic pressure plays an equal or dominant role in the evolution of the shock. The results of this problem at  $t = 0.05$  are shown in Fig. 8, where plots show density, pressure, magnitude of velocity and magnetic field strength in a cross section slice taken at  $z = 0$ . In addition the magnetic field lines are plotted on the magnetic field strength plot.

In this strong-field regime, the magnetic field lines are not significantly bent by the propagating blast wave but rather strongly constrain the blast wave into an oblate spheroidal shape. The density (and likewise pressure) enhancement in the shock is significantly reduced in the  $y$ -direction (left and top right panels) due to the additional pressure provided by the magnetic field which is compressed in this direction (bottom right panel).

### 4 Summary and conclusion

We have outlined several recent developments in smooth particle hydrodynamics. The equations of self-gravitating, ideal hydrodynamics were derived explicitly from a Lagrangian thereby yielding the correct particle index symmetries that ensure that the physical conservation laws are hard-wired into the discrete set of SPH equations without any arbitrariness. We have further

described the implementation of ideal MHD via so-called Euler potentials. This approach enforces the crucial  $\nabla \cdot \mathbf{B} = 0$ -constraint by construction. All dissipative terms required to capture discontinuities were carefully designed so that they a) have a form suggested in analogy with Riemann-solvers and b) are only active near discontinuities. These principles are implemented in our three-dimensional, Lagrangian magnetohydrodynamics code MAGMA. In a set of standard test problems used to benchmark numerical (magneto-)hydrodynamics schemes we have demonstrated the excellent performance of the code.

### Acknowledgement

DJP is supported by a UK Royal Society University Research Fellowship though much of this work has been funded by a PPARC/STFC postdoctoral fellowship.

Some of the results were visualized using SPLASH [69], a publicly available visualisation tool for SPH.

### References

1. S. Rosswog, E. Ramirez-Ruiz, and R. Hix, ApJ, accepted, arXiv:0712.2513 (2007).
2. S. Rosswog, E. Ramirez-Ruiz, and R. Hix, ApJ, submitted (2008).
3. S. Rosswog, M. Dan, E. Ramirez-Ruiz, and R. Hix, Computer Physics Communications, accepted (2007).
4. W. R. Hix, A. M. Khokhlov, J. C. Wheeler, and F.-K. Thielemann, ApJ **503**, 332 (1998).
5. L. Hernquist and N. Katz, ApJS **70**, 419 (1989).
6. W. Benz, in *Numerical Modeling of Stellar Pulsations*, edited by J. Buchler (Kluwer Academic Publishers, Dordrecht, 1990), p. 269.
7. J. J. Monaghan, Ann. Rev. Astron. Astrophys. **30**, 543 (1992).
8. R. Speith, Ph.D. thesis, Eberhard-Karls-Universität Tübingen, 1998.
9. J. J. Monaghan and D. J. Price, MNRAS **328**, 381 (2001).
10. V. Springel and L. Hernquist, MNRAS **333**, 649 (2002).
11. J. J. Monaghan, MNRAS **335**, 843 (2002).
12. L. Lucy, The Astronomical Journal **82**, 1013 (1977).
13. R. A. Gingold and J. J. Monaghan, MNRAS **181**, 375 (1977).
14. S. Gottloeber, G. Yepes, C. Wagner, and R. Sevilla, ArXiv Astrophysics e-prints (2006).
15. J. J. Monaghan, Reports of Progress in Physics **68**, 1703 (2005).
16. J. Monaghan and J. Lattanzio, A&A **149**, 135 (1985).
17. S. Rosswog and D. Price, MNRAS **379**, 915 (2007).
18. C. Eckart, Physics of Fluids **3**, 421 (1960).
19. D. Price, Ph.D. thesis, University of Cambridge, arXiv:astro-ph/0507472, 2004.
20. D. Price and J. Monaghan, MNRAS **374**, 1347 (2007).
21. G. Rüdiger and R. Hollerbach, *The magnetic universe : geophysical and astrophysical dynamo theory* (The Magnetic Universe: Geophysical and Astrophysical Dynamo Theory, by Günther Rüdiger, Rainer Hollerbach, pp. 343. ISBN 3-527-40409-0. Wiley-VCH, August 2004., ADDRESS, 2004).

22. T. E. Clarke, P. P. Kronberg, and H. Böhringer, *ApJL* **547**, L111 (2001).
23. L. M. Widrow, *Reviews of Modern Physics* **74**, 775 (2002).
24. M.-M. Mac Low and R. S. Klessen, *Reviews of Modern Physics* **76**, 125 (2004).
25. A. Heger, S. E. Woosley, and H. C. Spruit, *ApJ* **626**, 350 (2005).
26. C. Thompson and R. C. Duncan, *ApJ* **408**, 194 (1993).
27. T. Boyd and J. Sanderson, *The Physics of Plasmas* (Cambridge University Press, Cambridge, 2003).
28. D. J. Price and J. J. Monaghan, *MNRAS* **348**, 123 (2004).
29. J. Jackson, *Classical Electrodynamics*, 3. ed. (Wiley, New York, 1998).
30. H. Alfven, *Cosmical Electrodynamics* (Oxford University Press, Oxford, 1951).
31. L. Euler, *Novi Commentarii Acad. Sci. Petropolitanae* **14**, 270 (1769).
32. D. P. Stern, *Space Science Reviews* **6**, 147 (1966).
33. D. P. Stern, *American Journal of Physics* **38**, 494 (1970).
34. J. P. Morris, Ph.D. thesis, Monash University, Melbourne, Australia, 1996.
35. D. J. Price and J. J. Monaghan, *MNRAS* **364**, 384 (2005).
36. C. Ho, T. Huang, and S. Gao, *J. Geophys. Res.* **102**, 393 (1997).
37. C. Peymirat and D. Fontaine, *Ann. Geophysicae* **17**, 328 (1999).
38. S.-I. Inutsuka, *Journal of Computational Physics* **179**, 238 (2002).
39. S.-H. Cha and A. P. Whitworth, *MNRAS* **340**, 73 (2003).
40. D. J. Price, submitted to *Journal of Comp. Phys.*, arXiv0709.2772
41. J. J. Monaghan, *Journal of Computational Physics* **136**, 298 (1997).
42. J. Morris and J. Monaghan, *J. Comp. Phys.* **136**, 41 (1999).
43. J. E. Chow and J. Monaghan, *J. Computat. Phys.* **134**, 296 (1997).
44. L. Brookshaw, *Proceedings of the Astronomical Society of Australia* **6**, 207 (1985).
45. D. Heggie and P. Hut, *The Gravitational Million-Body Problem: A Multidisciplinary Approach to Star Cluster Dynamics* (The Gravitational Million-Body Problem: A Multidisciplinary Approach to Star Cluster Dynamics, by Douglas Heggie and Piet Hut. Cambridge University Press, 2003, 372 pp., ADDRESS, 2003).
46. T. Alexander, *Phys. Rep.* **419**, 65 (2005).
47. D. Price and S. Rosswog, *Science* **312**, 719 (2006).
48. S. Rosswog, *Rev. Mex. Astron. Astrophys.* **27**, 57 (2007).
49. H. Shen, H. Toki, K. Oyamatsu, and K. Sumiyoshi, *Nuclear Physics A* **637**, 435 (1998).
50. H. Shen, H. Toki, K. Oyamatsu, and K. Sumiyoshi, *Progress of Theoretical Physics* **100**, 1013 (1998).
51. S. Rosswog and M. B. Davies, *MNRAS* **334**, 481 (2002).
52. S. Rosswog and M. Liebendörfer, *MNRAS* **342**, 673 (2003).
53. W. Benz, R. Bowers, A. Cameron, and W. Press, *ApJ* **348**, 647 (1990).
54. S. Rosswog, M. B. Davies, F.-K. Thielemann, and T. Piran, *A&A* **360**, 171 (2000).
55. G. Sod, *J. Comput. Phys.* **43**, 1 (1978).
56. D. S. Balsara, *J. Comp. Phys.* **174**, 614 (2001).
57. V. Springel, *MNRAS* **364**, 1105 (2005).
58. M. Brio and C. C. Wu, *Journal of Computational Physics* **75**, 400 (1988).
59. J. M. Stone, J. F. Hawley, C. R. Evans, and M. L. Norman, *ApJ* **388**, 415 (1992).
60. W. Dai and P. R. Woodward, *J. Comp. Phys.* **115**, 485 (1994).

61. D. Ryu and T. W. Jones, *ApJ* **442**, 228 (1995).
62. D. S. Balsara, *ApJS* **116**, 133 (1998).
63. A. A. Barmin, A. G. Kulikovskiy, and N. V. Pogorelov, *J. Comp. Phys.* **126**, 77 (1996).
64. T. A. Gardiner and J. M. Stone, *J. Comp. Phys.* **205**, 509 (2005).
65. S. Orszag and C. Tang, *Journ. Fluid Mech.* **90**, 129 (1979).
66. R. B. Dahlburg and J. M. Picone, *Physics of Fluids B* **1**, 2153 (1989).
67. J. M. Picone and R. B. Dahlburg, *Physics of Fluids B* **3**, 29 (1991).
68. P. Londrillo and L. Del Zanna, *ApJ* **530**, 508 (2000).
69. D. J. Price, *Publications of the Astronomical Society of Australia* **24**, 159 (2007).